

Origin of local magnetic exchange interaction in infinite-layer nickelates

Yanbing Zhou^{1a}, Dan Zhao^{1a}, Boyun Zeng^{2a}, Chengliang Xia²,

Yu Wang¹, Hanghui Chen^{2,3b}, Tao Wu^{1,4,5,6b}, Xianhui Chen^{1,4,5,6b}

¹*Hefei National Research Center for Physical Sciences at the Microscale,
University of Science and Technology of China, Hefei 230026, China*

²*NYU-ECNU Institute of Physics, NYU Shanghai, Shanghai 200124, China*

³*Department of Physics, New York University, New York, New York 10012, USA*

⁴*Department of Physics, University of Science
and Technology of China, Hefei 230026, China*

⁵*Collaborative Innovation Center of Advanced Microstructures,
Nanjing University, Nanjing 210093, China*

⁶*Hefei National Laboratory, University of Science
and Technology of China, Hefei 230088, China*

^a These authors contributed equally to this work.

^b Correspondence to: hanghui.chen@nyu.edu, wutao@ustc.edu.cn, chenxh@ustc.edu.cn

Abstract

Significant magnetic exchange interactions have been observed in infinite-layer nickelates $R\text{NiO}_2$ ($R = \text{La, Pr, Nd}$), which exhibit unconventional superconductivity upon hole doping. Despite their structural and Fermi surface similarities to cuprates, infinite-layer nickelates possess a larger charge transfer gap, which influences their magnetic exchange interactions via oxygen. In this work, we performed ^{17}O nuclear magnetic resonance (NMR) measurements on LaNiO_2 and Sr-doped LaNiO_2 , revealing glassy spin dynamics originating from Ni-O planes. This indicates that infinite-layer nickelates are in proximity to magnetic ordering and that magnetic correlations play a crucial role in their physics. More importantly, our analysis of the Knight shift and hyperfine coupling of ^{17}O nuclei revealed that the Ni-Ni superexchange interaction, mediated by the σ bond between the Ni- $d_{x^2-y^2}$ and O- p orbitals, is one order of magnitude weaker than that in cuprates. This alone cannot account for the total magnetic exchange interaction observed in nickelates. First-principles many-body calculations indicate that an interstitial s orbital near the Fermi level, coupled with the Ni- $d_{3z^2-r^2}$ orbital, significantly enhances the superexchange interaction. This contrasts with cuprates, where magnetic interactions are predominantly governed by Cu- $d_{x^2-y^2}$ superexchange via oxygen. Our findings provide new insights into the distinct magnetic interactions in infinite-layer nickelates and their potential role in unconventional superconductivity.

Introduction

The discovery of superconductivity in infinite-layer nickelates $R\text{NiO}_2$ ($R = \text{La}, \text{Pr}, \text{Nd}$), has generated significant interest owing to their structural and electronic similarities to cuprates [1–4]. However, key differences between these two material families were recognized early in the study of nickel-based superconductors. One major distinction is that infinite-layer nickelates exhibit a substantially larger charge transfer gap than cuprates. As a direct consequence, the magnetic exchange interaction between neighboring $\text{Ni-}d_{x^2-y^2}$ spins—mediated via electron exchange through O- p orbitals (known as superexchange)—is expected to be significantly weaker than in cuprates. Reference [5] explicitly demonstrated that the σ -bond-driven superexchange in infinite-layer nickelates is an order of magnitude smaller than that in cuprates.

Nevertheless, strong antiferromagnetic correlations have been observed in infinite-layer nickelates via nuclear magnetic resonance (NMR), muon spin rotation (μSR), magnetic susceptibility and electronic Raman spectroscopy [6–10]. More importantly, resonant inelastic X-ray scattering (RIXS) measurements reveal dispersive magnetic excitations with a sizable exchange coupling of $J \sim 64$ meV between nearest-neighbor Ni spins—approximately half the value found in cuprates [11–15]. This apparent discrepancy between the theoretical predictions and experimental observations raises several fundamental questions: i) What role do O- p orbitals play in the superexchange mechanism of infinite-layer nickelates? ii) Is the total magnetic exchange coupling in nickelates solely governed by the σ bond between the $\text{Ni-}d_{x^2-y^2}$ and O- p orbitals, or do additional mechanisms contribute? iii) If other mechanisms are involved, which orbitals participate in the exchange process?

In this work, we combine NMR measurements with first-principles many-body calculations to address these questions. By performing ^{17}O NMR measurements on polycrystalline LaNiO_2 and $\text{La}_{1-x}\text{Sr}_x\text{NiO}_2$ samples, we found that the Ni–Ni superexchange interaction mediated by the σ bond between the $\text{Ni-}d_{x^2-y^2}$ and O- p orbitals accounts for only approximately 10% of that in cuprates, which is consistent with the theoretical expectations of Ref. [5]. This suggests that the σ -bond-driven superexchange alone is insufficient to explain the total magnetic exchange coupling observed in infinite-layer nickelates [11–15]. Furthermore, our first-principles many-body calculations reveal that the presence of an interstitial s orbital near the Fermi level, which hybridizes with the $\text{Ni-}d_{3z^2-r^2}$ orbital, significantly enhances

the superexchange in infinite-layer nickelates. This additional contribution to magnetic exchange is comparable in magnitude to the well-established $d_{x^2-y^2}$ - p σ -bond mechanism. Our results underscore the crucial role of low-energy interstitial s orbitals in the magnetic exchange interactions of infinite-layer nickelates, providing new insights into superexchange mechanisms of unconventional oxide superconductors.

^{17}O NMR spectroscopy

To conduct ^{17}O NMR measurements, we first synthesized an ^{17}O -enriched LaNiO_3 polycrystalline sample. Then, using CaH_2 as a reducing agent, the ^{17}O -enriched LaNiO_3 precursor is converted into the final ^{17}O -enriched LaNiO_2 polycrystalline sample [for details, see Sec. S1 in the Supplemental Information]. As shown in Figure 1(a), there is only one structural site for oxygen atoms in both stoichiometric LaNiO_3 and LaNiO_2 , which simplifies the present ^{17}O NMR investigation. A typical high-temperature ^{17}O NMR spectrum of the LaNiO_2 polycrystalline sample is shown in Fig. 1(c), which is significantly different from the ^{17}O NMR spectrum of polycrystalline LaNiO_3 (Fig. 1(b)). Considering the high spin number $I = 5/2$ of ^{17}O nuclei, both the quadrupole and magnetic hyperfine interactions experienced by ^{17}O nuclei determine the characteristics of the polycrystalline NMR spectrum. Our simulation of the polycrystalline NMR spectrum provides a quantitative understanding of the ^{17}O NMR spectra of both LaNiO_2 and LaNiO_3 , which indicates that the NMR parameters (electric field gradient (EFG) tensor and Knight shift) in LaNiO_2 are more anisotropic than those in LaNiO_3 [for details, see the captions of Fig. 1 and Sec. S2 in the Supplemental Information]. In addition, our simulation also indicates that the distribution of the quadrupole frequency ($\frac{\Delta\nu_q}{\nu_q}$) increases from $\sim 2\%$ to $\sim 6\%$ during the change from LaNiO_3 to LaNiO_2 , suggesting increased inhomogeneity from structural or charge degrees of freedom. As the temperature decreases, the ^{17}O NMR spectra exhibit a significant broadening effect at low temperatures (Fig. 1(d)), which smears out the characteristics of the ^{17}O NMR spectra and leads to increased uncertainty in the extracted NMR parameters. Therefore, we directly used the second central moment (M_2) of the ^{17}O NMR spectra to investigate the low-temperature broadening effect. As shown in Fig. 1(e), the temperature-dependent second central moment rapidly increases below ~ 70 K, suggesting possible electronic inhomogeneity. With the help of simulations of the broadening effect (Fig. 1(f)), we conclude

that the origin of such a broadening effect is dominated by magnetic contributions. In contrast, if the quadrupole contribution is predominant for the broadening effect, then the ^{17}O NMR spectrum always has a sharp central peak (Fig. 1(f)), which is inconsistent with our observations. Notably, strictly speaking, we cannot exclude a secondary quadrupole contribution to the total broadening effect. Our results clearly show that a predominant magnetic broadening effect appears in the ^{17}O NMR spectra below ~ 70 K, suggesting possible magnetic inhomogeneity at low temperatures. Previous AC susceptibility and μSR measurements of a LaNiO_2 polycrystalline sample revealed spin-glass behavior at low temperatures [8, 10], which provides a natural explanation for the observed magnetic broadening effect in the ^{17}O NMR spectra. Furthermore, we confirm that the magnetic broadening effect indeed comes from spontaneous internal fields due to the spin glass state, which leads to almost field-independent ^{17}O NMR spectra at low temperatures [for details, see Sec. S3 in the Supplemental Information]. In this work, we also synthesized an ^{17}O -enriched polycrystalline $\text{La}_{0.82}\text{Sr}_{0.18}\text{NiO}_2$ sample and performed ^{17}O NMR measurements. In Sr-doped LaNiO_2 , a similar spin-glass state is also observed in the temperature-dependent ^{17}O NMR spectra [for details, see Sec. S4 in the Supplemental Information]. Compared with that of pristine LaNiO_2 , the high-temperature ^{17}O NMR spectrum of $\text{La}_{0.82}\text{Sr}_{0.18}\text{NiO}_2$ has a wider distribution of NMR parameters [for details, see Sec. S4 in the Supplemental Information], suggesting an enhanced disorder effect due to the Sr dopants.

Glassy spin dynamics

To further investigate the spin-glass behavior, we measured the temperature-dependent spin-lattice relaxation rate ($1/T_1$), which probes the spectral density of spin fluctuations at the NMR frequency. Figure 2(a) shows the typical recovery curves of ^{17}O nuclear magnetization in both LaNiO_2 and $\text{La}_{0.82}\text{Sr}_{0.18}\text{NiO}_2$. To fit the recovery curves well, we use a stretched exponential formula, $M(t) = M_0 + M_1 \left(0.028e^{-\left(\frac{t}{T_1}\right)^\alpha} + 0.178e^{-\left(\frac{6t}{T_1}\right)^\alpha} + 0.794e^{-\left(\frac{15t}{T_1}\right)^\alpha} \right)$, which is widely used to describe the glassy spin dynamics of cuprates [16–30]. Here, the stretching exponent (α) reflects the distribution of spin-lattice relaxation times (T_1) and serves as a key indicator of glassy spin dynamics. In cuprates, the glassy spin dynamics are well captured by the Bloembergen–Purcell–Pound (BBP) mechanism [19, 24, 31, 32], which assumes that the autocorrelation function of the fluctuating hyperfine field $h(t)$ decays expo-

nentially with time (t): $\langle h(t)h(0) \rangle = \langle h^2 \rangle e^{-t/\tau_c}$ [33]. Accordingly, the spin-lattice relaxation rate is given by $\frac{1}{T_1} = \gamma_N^2 \langle h_\perp^2 \rangle \frac{2\tau_c}{1+\omega_N^2\tau_c^2}$, where τ_c is the correlation time between local spins and is assumed to decrease with temperature as $\tau_c = \tau_\infty e^{E/k_B T}$. Here, the activation energy (E) is assumed to be temperature independent, h_\perp is the transverse fluctuating field at the nuclear site, and γ_N is the gyromagnetic ratio of the nuclei. Within this framework, as the correlation time increases with cooling, the value of $1/T_1$ reaches a maximum when $\tau_c \sim \omega_N$. The temperature of the maximum $1/T_1$ defines the freezing temperature (T_{1f}) on the NMR timescale.

As shown in Fig. 2(b), the temperature-dependent $1/T_1$ exhibits broad peak-like behavior at low temperatures in both LaNiO_2 and $\text{La}_{0.82}\text{Sr}_{0.18}\text{NiO}_2$, which supports the spin freezing of local spins and defines the characteristic freezing temperature T_{1f} (~ 52 K for LaNiO_2 and ~ 26 K for $\text{La}_{0.82}\text{Sr}_{0.18}\text{NiO}_2$). Moreover, the stretching exponent α becomes much smaller than 1 at low temperatures (Fig. 2(c)), indicating a remarkable inhomogeneity of spin dynamics in the spin-glass state. On the other hand, the overall temperature dependence of $1/T_1$ suggests that the local spins in the system are only partially frozen. By further qualitative analysis [for details, see Sec. S5 in the Supplemental Information], $1/T_1$ can be decomposed into two contributions: one is the spin freezing component $(1/T_1)_{\text{BPP}}$, which is well described by the BPP model, and the other is a paramagnetic component $(1/T_1)_{\text{para}}$, which continuously decreases with decreasing temperature and represents unfrozen spins with strong antiferromagnetic correlations [6]. Notably, while the peak temperature of $1/T_1$ in $\text{La}_{0.82}\text{Sr}_{0.18}\text{NiO}_2$ is much lower than that in LaNiO_2 , Sr doping significantly enhances the magnitude of the peak in $1/T_1$ (Fig. 2(b)), implying an increase of the frozen spins. This observation suggests a dual role of Sr doping in glassy spin dynamics. On the one hand, the Sr dopants enhance chemical/structural disorder, which leads to an increase of frozen spins. On the other hand, Sr doping introduces additional holes, which alter the activation energy for spin glass. More evidence for glassy spin dynamics is also provided by ^{139}La NMR, where the peak behavior in $1/T_1$ clearly exhibits frequency dependence, as expected by the BPP model [for details, see Sec. S5 in the Supplemental Information].

Further measurement of the nuclear spin-spin relaxation rate $1/T_2$, which measures slow longitudinal field fluctuations, also supports a spin-glass state at low temperatures. The nuclear spin-spin relaxation time T_2 was extracted by fitting the spin-echo decay curves via the formula $S(\tau) = S_0 e^{-\left(\frac{2\tau}{T_2}\right)^\beta}$ (Fig. 2(d)), where the factor $\beta < 1$ accounts for a

distribution of T_2 values [34]. As shown in Fig. 2(e), the temperature-dependent $1/T_2$ develops a pronounced broad peak at low temperatures, which is a typical characteristic of the spin-glass state. Similar to the results of $1/T_1$, Sr doping leads to an enhanced peak in $1/T_2$, supporting an increase of the frozen spins. In addition, the stretching factor β clearly decreases around the peak region (Fig. 2(f)), which is consistent with glassy spin dynamics.

Superexchange mediated by the σ bond

The observed spin-glass behavior in infinite-layer nickelates resembles that in underdoped cuprates [16–30], in which carrier doping suppresses long-range magnetic order but a glassy magnetic state persists [19, 24, 31, 32, 35–38]. In infinite-layer nickelates, while self-doping disrupts the establishment of long-range magnetic order [39], significant antiferromagnetic correlations persist, which leads to the observed spin-glass state [6–15]. Usually, the strong antiferromagnetic correlations among Ni spins are ascribed to the superexchange mediated by the O- p orbital. The present ^{17}O NMR measurement can offer a unique chance to investigate this kind of superexchange. In $3d$ transition metal compounds, the effective superexchange interaction strength J is related to the charge transfer gap Δ_{pd} and is expressed as $J = \frac{4t_{pd}^4}{\Delta_{pd}^2} \left(\frac{1}{U_{dd}} + \frac{1}{\Delta_{pd} + \frac{U_{pp}}{2}} \right)$ [40]. Previous ^{17}O NMR experiments on cuprates have established that the hyperfine coupling constant of ^{17}O directly reflects the hybridization between O- p and Ni- d orbitals, which is influenced by the charge transfer gap Δ_{pd} [41]. Therefore, analysis of the hyperfine coupling of ^{17}O can provide a qualitative estimation of the superexchange interactions mediated by the σ bond between the Ni- $d_{x^2-y^2}$ and O- p orbitals in our case.

By analysing the high-temperature ^{17}O NMR spectra of LaNiO_2 , we can extract the Knight shifts of ^{17}O along three crystallographic directions. As shown in Figure 3(d), the temperature-dependent Knight shift decreases continuously with cooling, which is quite consistent with the previous ^{139}La NMR results [6]. In principle, the total Knight shift can be expressed as $K_i = K_i^{\text{orb}} + A_i \chi_i$, where $i = a, b$, and c , K_i^{orb} is temperature-independent orbital shift, A_i is the hyperfine coupling constant of ^{17}O , and χ_i is the bulk spin susceptibility. Specifically, without considering spin-orbit coupling, the hyperfine coupling constant of ^{17}O consists of two components: $A_i = A^{\text{iso}} + A_i^{\text{dip}}$. The isotropic term A^{iso} originates from the Fermi contact interaction due to the hybridization between the Ni- d and O- $2s$

orbitals. The anisotropic term A^{dip} arises from the dipolar interaction, obeying the relation $A_b^{\text{dip}} = -2A_a^{\text{dip}} = -2A_c^{\text{dip}}$. The dipolar contribution is closely related to the pd -hybridization and is given by $A_b^{\text{dip}} = 2f_{p\sigma}\alpha_p$, $A_a^{\text{dip}} = A_c^{\text{dip}} = -f_{p\sigma}\alpha_p$, where $\alpha_p = \frac{4}{5}\hbar\gamma\mu_B\langle r^{-3}\rangle$ represents the dipolar contribution from the $2p$ orbital, and $f_{p\sigma}$ is the so-called “spin density”, which gives the statistical weight of the hybridized wave function in the ligand orbitals with $f_{p\sigma}$ character [41]. Typically, $f_{p\sigma} \propto \frac{t_{pd}^2}{\Delta_{pd}^2}$, where t_{pd} is the hopping integral between O- p orbitals and Ni- $d_{x^2-y^2}$ orbitals and where Δ_{pd} is the energy difference between these orbitals [41]. Given that the superexchange interaction between the localized spins on Ni- $d_{x^2-y^2}$ orbitals is mediated by O- $2p_\sigma$ bonds (Fig. 3(a)), we can estimate the strength of this superexchange interaction by analysing the hyperfine coupling constants of oxygen A_i . By comparing the Knight shifts along different crystallographic directions (Fig. 3(e)), we determined the anisotropy ratio of the hyperfine coupling constant, $\frac{\Delta K_b}{\Delta K_c} = \frac{A_b}{A_c} = \frac{A^{\text{iso}} + A_b^{\text{dip}}}{A^{\text{iso}} - \frac{1}{2}A_b^{\text{dip}}} \sim 1.11$, which is significantly smaller than that of ~ 1.6 in cuprates (Fig. 3(f)). Given the comparable t_{pd} values for nickelates and cuprates, this smaller anisotropy ratio suggests a larger charge-transfer gap Δ_{pd} in nickelates than in cuprates.

To analyse the charge-transfer energy Δ_{pd} more quantitatively, we measured the bulk magnetic susceptibility χ and evaluated the $K - \chi$ relationship to extract the hyperfine coupling constants A_i [for details, see Secs. S6 and S7 in the Supplemental Information]. Finally, we obtain $A_a \sim 16.1$ kOe/ μ_B , $A_b \sim 18.9$ kOe/ μ_B , and $A_c \sim 15.2$ kOe/ μ_B . The dipolar contribution, which is calculated by $A_b^{\text{dip}} = A_b - \frac{A_a + A_b + A_c}{3} \sim 2.2$ kOe/ μ_B , is much smaller than that in $\text{YBa}_2\text{Cu}_3\text{O}_{7-\delta}$ ($A_b^{\text{dip}} \sim 20.7$ kOe/ μ_B) [42, 43]. By calculating the ratio $\frac{\Delta_{pd}^{\text{Ni}}}{\Delta_{pd}^{\text{Cu}}} \sim \left(\frac{(A_b^{\text{dip}})^{\text{Cu}}}{(A_b^{\text{dip}})^{\text{Ni}}} \right)^{\frac{1}{2}} \sim 3.1$, we conclude that the charge-transfer gap in LaNiO_2 is three times larger than that in cuprates. Furthermore, the ratio of superexchange interactions

in cuprates and LaNiO_2 can be estimated by $\frac{J_{\text{Cu}}^{\text{Cu}}}{J_{\text{Ni}}^{\text{Cu}}} = \frac{\left(\frac{1}{\Delta_{pd}^2}\right)_{\text{Cu}}}{\left(\frac{1}{\Delta_{pd}^2}\right)_{\text{Ni}}} \cdot \frac{\left(\frac{1}{U_{dd}} + \frac{1}{\Delta_{pd} + \frac{1}{2}U_{pp}}\right)_{\text{Cu}}}{\left(\frac{1}{U_{dd}} + \frac{1}{\Delta_{pd} + \frac{1}{2}U_{pp}}\right)_{\text{Ni}}} \sim 10$.

Here, we assume that $U_{dd}^{\text{Ni}} \sim U_{dd}^{\text{Cu}}$ and that $U_{pp}^{\text{Ni}} \sim U_{pp}^{\text{Cu}}$. Since the superexchange interaction in cuprates typically ranges from 100 meV to 180 meV (e.g., $J \sim 140$ meV in $\text{YBa}_2\text{Cu}_3\text{O}_{7-\delta}$) [44, 45], we estimate that the superexchange interaction in LaNiO_2 is approximately 10–18 meV. This value is substantially lower than the $J \sim 64$ meV extracted from RIXS experiments in both infinite-layer nickelate thin films and bulk samples [11–15].

In infinite-layer nickelates, as illustrated in Fig. 3(b-c), the O- p orbitals are farther from the Fermi level compared to cuprates, and the charge transfer gap Δ_{pd} is larger than the

onsite Coulomb repulsion U of Ni- d electrons [5, 46, 47]. This difference leads to a larger charge transfer gap Δ_{pd} in infinite-layer nickelates than in cuprates [5, 46]. According to the Zaanen–Sawatzky–Allen (ZSA) classification [40], infinite-layer nickelates are categorized as Mott–Hubbard-type insulators, whereas cuprates are charge-transfer insulators. As Δ_{pd} increases, it is reasonable to infer that the σ bond between the Ni- $d_{x^2-y^2}$ and O- p_x orbitals plays a less significant role in mediating the magnetic exchange interactions in infinite-layer nickelates than does its dominant role in cuprates. Our present ^{17}O NMR results strongly support this conjecture. Considering that the total superexchange interaction in infinite-layer nickelates has a moderate value ($J \sim 64$ meV), we propose that, in addition to the well-established σ bond between the Ni- $d_{x^2-y^2}$ and O- p orbitals, other virtual hopping pathways also contribute substantially to the total magnetic interaction in infinite-layer nickelates.

Theoretical modeling of the superexchange

We now explain how additional orbitals and extended hopping pathways may appreciably increase the total magnetic exchange of infinite-layer nickelates. Figure 4(a) shows the well-known $d_{x^2-y^2}$ - p_x - $d_{x^2-y^2}$ cluster model (hereafter referred to as the pd model) that is widely used to estimate the superexchange mediated by the pd σ bond [40]. To better account for the full superexchange in infinite-layer nickelates, we extend the pd model to a new cluster model, shown in Fig. 4(b). We refer to it as the pds model. Our previous first-principles calculations revealed a key distinction between infinite-layer nickelates and cuprates: the presence of an interstitial s orbital in the former, with its energy lying close to the Fermi level [48]. In the pds model, we incorporate the interstitial s orbital. In addition, we include the Ni- $d_{3z^2-r^2}$ orbital, motivated by the fact that in the presence of the interstitial s orbital, the bare energies of the $d_{x^2-y^2}$ and $d_{3z^2-r^2}$ orbitals become nearly degenerate [48–50]. As a result, a new σ bonding pathway emerges, formed between the Ni- $d_{3z^2-r^2}$ and interstitial s orbitals, in addition to the well-known $d_{x^2-y^2}$ - p_x σ bond. We adopt open boundary conditions [51, 52], such that each Ni site is flanked by two interstitial s orbitals. All symmetry-allowed nearest-neighbor hoppings are included in the pds model, as explicitly shown in Fig. 4(b). The onsite orbital energies and hopping parameters are extracted from first-principles calculations and Wannier fitting. We apply a full Slater-Kanamori interaction to each Ni site [53]. Based on our DMFT calculations, we choose a representative interaction strength of $U = 5.0$ eV

and Hund’s coupling $J_H = 1.0$ eV, which reproduce the mass enhancement of Ni d orbitals obtained from GW+EDMFT simulations [54]. We also explore a range of U and J_H values around these benchmarks. The complete Hamiltonian for the pds cluster model is presented in the Methods. Following Ref. [40], we compare a “ferromagnetic” (FM) configuration with total spin projection $S_z = 1$ and an “antiferromagnetic” (AFM) configuration with $S_z = 0$. To represent the formal valence states of Ni^{1+} and O^{2-} in infinite-layer nickelates, we set the total number of electrons in the pds model to $N_e = 8$.

We next perform exact diagonalization of the “FM” and “AFM” Hamiltonians in the corresponding many-body basis to obtain the respective ground-state energies, E_{FM} and E_{AFM} . Since the model effectively describes two coupled spin- $\frac{1}{2}$ degrees of freedom, the magnetic exchange interaction can be mapped onto a spin- $\frac{1}{2}$ Heisenberg model and the superexchange coupling is obtained by $J = |E_{\text{FM}} - E_{\text{AFM}}|$ [40] (see the Methods for more details). Owing to the larger phase space available in the “AFM” configuration, we consistently find $E_{\text{AFM}} < E_{\text{FM}}$. A key result of our analysis is that the energy of the interstitial s orbital serves as a critical control parameter for tuning the superexchange strength. We define Δ_s as the onsite energy difference between the interstitial s orbital and the Ni- $d_{x^2-y^2}$ orbital. In Fig. 4(c), we plot the dependence of J on Δ_s for several values of the Hubbard interaction U , keeping the Hund’s coupling fixed at $J_H = 0.2U$. A complementary analysis in Fig. 4(d) explores the variation of J with J_H at fixed $U = 5$ eV. In both cases, we find that J increases significantly as Δ_s decreases. In particular, when Δ_s is appreciably smaller than U (shaded region), the interstitial s orbital becomes energetically relevant and substantially enhances the superexchange. For large Δ_s (e.g., 10 eV), the s orbital lies far above the Fermi level and its contribution to the superexchange vanishes, resulting in a saturated $J \approx 20$ meV. In contrast, when Δ_s is set to its first-principles value of approximately 2.6 eV, the superexchange increases markedly, with J reaching values in the range of 50–120 meV, depending on the interaction parameters. While the pds model is still simplified and not intended to yield quantitative estimate of superexchange, it provides compelling evidence that the combined involvement of the interstitial s orbital and the Ni $d_{x^2-y^2}$ and $d_{3z^2-r^2}$ orbitals can strongly enhance the magnetic exchange interactions in infinite-layer nickelates.

Discussions and conclusions

In high- T_c superconductors, antiferromagnetic spin fluctuations are widely recognized as central to the mechanism of unconventional pairing [55, 56]. While a precise theoretical prediction of the superconducting transition temperature (T_c) remains challenging, numerous studies suggest that the strength of these spin fluctuations imposes an upper bound on T_c [44, 57]. This has led to the view that enhancing the magnetic exchange interaction J —which governs spin fluctuation strength—may be a viable route to higher T_c . In cuprates, J arises primarily from superexchange via oxygen p orbitals, and is inversely related to the charge transfer gap Δ_{pd} between oxygen p and copper d states. The empirical correlation between smaller Δ_{pd} and higher T_c within the $\text{Bi}_2\text{Sr}_2\text{Ca}_{n-1}\text{Cu}_n\text{O}_{2n+4+\delta}$ series underscores this link [57].

Our study extends this framework to infinite-layer nickelates, where we identify both similarities and crucial differences in the origin of magnetic interactions. In particular, we find that the well-known $d_{x^2-y^2}$ - p σ -bond superexchange is not the dominant contributor to J in these superconductors. Instead, we highlight the significant role of a distinct exchange pathway involving the interstitial- s orbital, which has negligible impact in cuprates due to its high energy. We show that lowering the energy of this orbital—through structural or chemical tuning—can substantially enhance magnetic coupling. This mechanism offers a plausible explanation for the elevated T_c values recently reported in $(\text{Sm-Eu-Ca-Sr})\text{NiO}_2$ thin films [58], where enhanced interstitial- s participation may amplify the effective superexchange interaction.

In conclusion, our ^{17}O NMR measurements on infinite-layer nickelates reveal that the conventional in-plane σ -bond-mediated superexchange is significantly weaker than in cuprates, consistent with the larger charge transfer gap of infinite-layer nickelates. However, this alone cannot account for the full magnitude of the magnetic exchange coupling observed experimentally [11–15]. Through cluster model calculations, we identify a novel exchange channel involving the interstitial- s , $\text{Ni-}d_{3z^2-r^2}$, and $\text{O-}p$ orbitals, which contributes substantially to J in nickelates but is negligible in cuprates. These results establish a key distinction in the magnetic physics of nickelates and suggest a broader design principle: magnetic interactions—and by extension, superconductivity—in oxide materials can be engineered by manipulating the energies and hybridizations of non-canonical orbitals near the Fermi level.

Methods

Sample Preparation

Powder samples of LaNiO_3 and Sr-doped LaNiO_3 were synthesized via a sol-gel method [59]. Stoichiometric amounts of metal nitrates were mixed to prepare the desired LaNiO_3 and $\text{La}_{0.8}\text{Sr}_{0.2}\text{NiO}_3$ precursor solutions with excess citric acid. The solution was slowly evaporated until it became green gel, which was then burned at $\sim 500^\circ\text{C}$ for several hours to yield gray precursor powder. These precursors of LaNiO_3 and $\text{La}_{0.8}\text{Sr}_{0.2}\text{NiO}_3$ were subsequently calcined at 950°C for 12 h. The LaNiO_3 precursor was calcined in flowing O_2 , whereas the $\text{La}_{0.8}\text{Sr}_{0.2}\text{NiO}_3$ precursor required an O_2 pressure of ~ 120 bar to stabilize the desired perovskite 113 phase.

For subsequent ^{17}O NMR measurements, the synthesized oxide powders were ^{17}O isotopically enriched. Powder LaNiO_3 was enriched by annealing at 900°C for 102 h in a $^{17}\text{O}_2$ atmosphere. Similarly, powder samples of Sr-doped LaNiO_3 were enriched by annealing at 710°C for 120 h in a $^{17}\text{O}_2$ atmosphere. Polycrystalline samples of the infinite-layer nickelates, LaNiO_2 and Sr-doped LaNiO_2 , were then obtained by chemical reduction of these ^{17}O -enriched samples of LaNiO_3 and Sr-doped LaNiO_3 using CaH_2 as the reducing agent [60]. The actual stoichiometry of the Sr-doped final product was confirmed to be $\text{La}_{0.82}\text{Sr}_{0.18}\text{NiO}_2$ through inductively coupled plasma-mass spectrometry (ICP-MS).

NMR Experiments

To perform NMR measurements on both parent and doped samples, each isotope enriched sample was filled with a copper coil and then sealed with epoxy adhesive. A commercial NMR spectrometer from Thamway Co. Ltd was used for the NMR measurements. The external magnetic field at the sample position was calibrated by the ^{63}Cu resonance frequency of the copper coil. All ^{139}La and ^{17}O NMR signals were measured via the standard spin echo method using the $\pi/2-\tau-\pi-\tau$ pulse sequence; subsequently, the time-domain signals were converted to spectra via fast Fourier transform, and these spectra were summed to obtain a full spectrum.

We carried out nuclear spin-lattice relaxation time (T_1) measurements on ^{139}La and

^{17}O nuclei using comb $\pi/2$ -pulse for saturation, followed by the t_j - $\pi/2$ - τ - π - τ pulse sequence, where t_j varies, and we can plot the integral signal intensity I_s versus t_j . Since I_s is proportional to magnetization intensity M , we fit the data with formulas $M(t) = M_0 + M_1 \left(\frac{1}{84}e^{-\left(\frac{t}{T_1}\right)^\alpha} + \frac{3}{44}e^{-\left(\frac{6t}{T_1}\right)^\alpha} + \frac{75}{364}e^{-\left(\frac{15t}{T_1}\right)^\alpha} + \frac{1225}{1716}e^{-\left(\frac{28t}{T_1}\right)^\alpha} \right)$ for ^{139}La and $M(t) = M_0 + M_1 \left(0.028e^{-\left(\frac{t}{T_1}\right)^\alpha} + 0.178e^{-\left(\frac{6t}{T_1}\right)^\alpha} + 0.794e^{-\left(\frac{15t}{T_1}\right)^\alpha} \right)$ for ^{17}O , where t is recovery time, and α is stretch exponent describing a distribution of T_1 . We extracted T_1 and α from the fitting. Nuclear spin-spin relaxation time (T_2) measurements were performed with the $\pi/2$ - τ - π - τ pulse sequence, and we collected the data under different τ value; similarly, we can plot I_s versus τ and fit the data with the formula $m(\tau) = m_0 + m_1e^{-\left(\frac{\tau}{T_2}\right)^\beta}$ to obtain T_2 and β for both ^{139}La and ^{17}O .

Density Functional Theory (DFT) calculations

We perform density functional theory (DFT) calculations [61, 62], implemented in Vienna ab initio simulation package (VASP) code [63] with projector augmented wave (PAW) method [64]. We use Perdew-Burke-Ernzerhof (PBE) [65] exchange-correlation functional. We use an energy cutoff of 600 eV and sample the Brillouin zone by using Γ -centered \mathbf{k} -mesh of $14 \times 14 \times 14$ per primitive cell. The total energy convergence criterion is 10^{-6} eV. The force convergence criterion is 1 meV/Å. The pressure convergence criterion is 0.1 kbar. The empty La-4*f* orbitals are included in the pseudopotential and we use an on-site Coulomb interaction $U_{\text{La-4}f} = 10$ eV to move the La-*f* orbitals away from the Fermi level. We use maximally-localized-Wannier-function [66], implemented in Wannier90 [67], to fit the DFT band structure of LaNiO_2 by the 17-orbital model that includes one interstitial *s* orbital, five La-*d* orbitals, five Ni-*d* orbitals, and six O-*p* orbitals. The Wannier fitting perfectly reproduces the DFT bands structure in an energy window of about 15 eV around the Fermi level (see Fig. S1 in the Supplementary Information). Based on the Wannier fitting, we extract the hopping matrix elements $t_{\alpha\beta}$ and onsite energy differences Δ_α that will be used in the cluster model calculation for the superexchange of LaNiO_2 .

Based on the 17-orbital model described above, we perform dynamical mean-field theory (DMFT) calculations [68, 69] to study the mass enhancement of the two Ni- e_g orbitals in LaNiO₂. The impurity problem is solved using the hybridization-expansion continuous-time quantum Monte Carlo (CTQMC) algorithm [70, 71], as implemented in the code developed by K. Haule [72]. At each DMFT iteration, we collect a total of 2 billion Monte Carlo samples to ensure convergence of the impurity Green's function and self-energy. The calculations are performed at a temperature of 116 K. We employ a Slater-Kanamori interaction on the Ni- d orbitals [73] and the fully localized limit (FLL) form for the double counting correction [74]. The two Ni- e_g orbitals are treated dynamically within DMFT, while the filled Ni- t_{2g} shell is handled at the static Hartree-Fock level. Because the system is metallic, the quasiparticle weight Z , defined via the real part of the retarded self-energy, can be used to estimate the mass enhancement:

$$\frac{m^*}{m} \approx \frac{1}{Z} = 1 - \frac{1}{\hbar} \frac{\partial \text{Re } \Sigma(\omega)}{\partial \omega} \Big|_{\omega=0} \quad (1)$$

Here, $\omega = 0$ denotes the chemical potential. Since CTQMC yields the self-energy on the Matsubara axis, we infer the low-frequency behavior under the assumption of Fermi-liquid behavior, which allows us to estimate Z from the imaginary part of the self-energy at low Matsubara frequencies [75]:

$$\frac{m^*}{m} \approx \frac{1}{Z} \approx 1 - \frac{1}{\hbar} \frac{\partial \text{Im } \Sigma(i\omega_n)}{\partial \omega_n} \Big|_{\omega_n \rightarrow 0} \quad (2)$$

In practice, we fit a fourth-order polynomial to the first six Matsubara-frequency points of $\text{Im}\Sigma(i\omega_n)$ and compute the derivative from this fit. For $U = 5$ eV and $J_H = 0.2U$, we obtain a mass enhancement of 5.4 for the Ni- $d_{x^2-y^2}$ orbital, in agreement with previous GW+EDMFT results [54]. We therefore adopt $U = 5$ eV and $J_H = 0.2U$ as representative interaction parameters. The corresponding Matsubara self-energy is shown in Fig. S6 of the Supplementary Information. We have verified that the main conclusions remain robust across a range of U and J_H values.

We extend the classical three-orbital pd model to a pds model, schematically illustrated in Fig. 4(b). This model comprises nine orbitals: two $\text{Ni-}d_{x^2-y^2}$ orbitals, two $\text{Ni-}d_{3z^2-r^2}$ orbitals, one $\text{O-}p_x$ orbital, and four interstitial s orbitals. The model is defined by the Hamiltonian:

$$\hat{H} = \hat{H}_0 + \hat{H}_{\text{int}}, \quad (3)$$

where \hat{H}_0 is the tight-binding part:

$$\begin{aligned} \hat{H}_0 = & \sum_{\sigma} \Delta_{p_x} \hat{c}_{p_x\sigma}^{\dagger} \hat{c}_{p_x\sigma} + \sum_{i=\{1,2\}}^{\sigma} \Delta_{d_z} \hat{c}_{i,d_z\sigma}^{\dagger} \hat{c}_{i,d_z\sigma} + \sum_{j=\{1t, 1b, 2t, 2b\}}^{\sigma} \Delta_s \hat{c}_{j,s\sigma}^{\dagger} \hat{c}_{j,s\sigma} \\ & + \sum_{i=\{1,2\}}^{\sigma} t_{p_x d_x} \left((-1)^i \hat{c}_{i,d_x\sigma}^{\dagger} \hat{c}_{p_x\sigma} + \text{h.c.} \right) + \sum_{i=\{1,2\}}^{\sigma} t_{p_x d_z} \left((-1)^i \hat{c}_{i,d_z\sigma}^{\dagger} \hat{c}_{p_x\sigma} + \text{h.c.} \right) \\ & + \sum_{j=\{1t, 1b\}}^{\sigma} t_{sd_z} \left(\hat{c}_{j,s\sigma}^{\dagger} \hat{c}_{1,d_z\sigma} + \text{h.c.} \right) + \sum_{j=\{2t, 2b\}}^{\sigma} t_{sd_z} \left(\hat{c}_{j,s\sigma}^{\dagger} \hat{c}_{2,d_z\sigma} + \text{h.c.} \right) \\ & + \sum_{j=\{1t, 1b\}}^{\sigma} t_{sp_x} \left(\hat{c}_{j,s\sigma}^{\dagger} \hat{c}_{p_x\sigma} + \text{h.c.} \right) + \sum_{j=\{2t, 2b\}}^{\sigma} (-t_{sp_x}) \left(\hat{c}_{j,s\sigma}^{\dagger} \hat{c}_{p_x\sigma} + \text{h.c.} \right) \end{aligned} \quad (4)$$

Here, “1” and “2” label the two Ni sites, and “t” and “b” refer to “top” and “bottom”. \hat{H}_{int} is a Slater–Kanamori interaction on the d orbitals of both Ni sites:

$$\begin{aligned} \hat{H}_{\text{int}} = & \sum_{\substack{i=\{1,2\} \\ \nu=d_x, d_z}} U \hat{n}_{i,\nu\uparrow} \hat{n}_{i,\nu\downarrow} + \sum_{\substack{\sigma\sigma' \\ i=\{1,2\}}} (U' - J_H \delta_{\sigma\sigma'}) \hat{n}_{i,d_x\sigma} \hat{n}_{i,d_z\sigma'} \\ & + \sum_{i=\{1,2\}} (-J_H) \left(\hat{c}_{i,d_z\downarrow}^{\dagger} \hat{c}_{i,d_x\uparrow}^{\dagger} \hat{c}_{i,d_x\downarrow} \hat{c}_{i,d_z\uparrow} + \text{h.c.} \right) \\ & + \sum_{i=\{1,2\}} (-J') \left(\hat{c}_{i,d_z\downarrow}^{\dagger} \hat{c}_{i,d_z\uparrow}^{\dagger} \hat{c}_{i,d_x\downarrow} \hat{c}_{i,d_x\uparrow} + \text{h.c.} \right) \end{aligned} \quad (5)$$

Here, d_x (d_z) denotes $\text{Ni-}d_{x^2-y^2}$ ($\text{Ni-}d_{3z^2-r^2}$) orbital. The operator $\hat{c}_{i,\nu\sigma}^{\dagger}$ creates an electron at site i in orbital ν with spin σ . “h.c.” indicates the Hermitian conjugate. The model parameters are defined as follows: in \hat{H}_0 , Δ_{α} is the onsite energy of orbital α relative to $\text{Ni-}d_{x^2-y^2}$ (thus $\Delta_{d_x} = 0$ and is not shown); $t_{\alpha\beta}$ denotes the nearest-neighbor hopping between orbitals α and β . In \hat{H}_{int} , U is the intra-orbital Coulomb interaction, U' is the inter-orbital interaction, J_H is the Hund’s coupling, and J' is the pair-hopping term. To preserve spin $\text{SU}(2)$ symmetry, we set $U' = U - 2J_H$ and $J' = J_H$. The values of Δ_{α} and $t_{\alpha\beta}$ are listed in Table I.

TABLE I. Model parameters. d_x (d_z) denotes Ni- $d_{x^2-y^2}$ (Ni- $d_{3z^2-r^2}$) orbital. Δ_α is the onsite energy of orbital α relative to Ni- $d_{x^2-y^2}$; $t_{\alpha\beta}$ is the hopping between orbitals α and β . Units are in eV.

Δ_{p_x}	Δ_s	Δ_{d_z}	
-3.77	2.59	-0.04	
$t_{p_x d_x}$	$t_{p_x d_z}$	$t_{s p_x}$	$t_{s d_z}$
1.27	0.66	0.57	1.08

In the pds model with $N_{\text{orb}} = 9$, we set the total electron number to $N_e = 8$. This reflects the nominal d^9 configuration of Ni in LaNiO_2 , corresponding to three electrons in the two e_g orbitals on each Ni site. The O- p_x orbital is formally filled with two electrons, and the interstitial s orbitals are nominally empty. Since the system effectively contains two coupled spin- $\frac{1}{2}$ moments, we define “ferromagnetic” and “antiferromagnetic” configurations as follows.

For the “ferromagnetic” configuration, we fix the total spin projection $S_z = 1$, resulting in $N_e^\uparrow = 5$ and $N_e^\downarrow = 3$. The corresponding many-body Hilbert space has dimension $C_{N_{\text{orb}}}^{N_e^\uparrow} \times C_{N_{\text{orb}}}^{N_e^\downarrow} = 10,584$. For the “antiferromagnetic” configuration, we set $S_z = 0$, giving $N_e^\uparrow = N_e^\downarrow = 4$, and a Hilbert space dimension of 15,876.

We construct the Hamiltonian in Eq. (3) within both configurations and perform exact diagonalization to obtain the ground-state energies E_{FM} and E_{AFM} . We then map the pds model onto a spin- $\frac{1}{2}$ Heisenberg model, $H = J\mathbf{S}_1 \cdot \mathbf{S}_2$, where the energy difference between the spin-singlet and spin-triplet states is $-J$. Therefore, the superexchange coupling is determined as $J = |E_{\text{FM}} - E_{\text{AFM}}|$, with $E_{\text{AFM}} < E_{\text{FM}}$.

Acknowledgements

We acknowledge useful discussions with Mi Jiang, Mona Berciu and George A. Sawatzky. This work is supported by the National Key R&D Program of the MOST of China (Grant No. 2022YFA1602601), the National Natural Science Foundation of China (Grants No. 12034004, 12161160316, 12325403, 12488201, 12204450), the Chinese Academy of Sciences under contract No. JZHKYPT-2021-08, the CAS Project for Young Scientists in Basic

Research (Grant No. 2022YSBR-048), the Innovation Program for Quantum Science and Technology (Grant No. 2021ZD0302800), and the Fundamental Research Funds for the Central Universities (No. WK9990000110). H.H.C. was financially supported by the National Natural Science Foundation of China under project number 12374064 and 12434002, Science and Technology Commission of Shanghai Municipality under grant number 23ZR1445400 and a grant from the New York University Research Catalyst Prize under project number RB627. C.L.X. was supported by the National Natural Science Foundation of China under project number 12404082. NYU High-Performance-Computing (HPC) provides computational resources.

Author contributions

X.H.C., T.W. and H.H.C. conceived the project. Y.B.Z., D.Z. and Y.W. performed NMR experiments. Y.B.Z. grew the samples with the help of D.Z.. B.Y.Z., C.L.X. and H.H.C. performed theoretical calculations. Y.B.Z., D.Z. and T.W. analysed the NMR data. Y.B.Z., D.Z., H.H.C. and T.W. wrote the manuscript with input from all the authors. All authors discussed the results and commented on the manuscript.

Competing interests

The authors declare no competing interests.

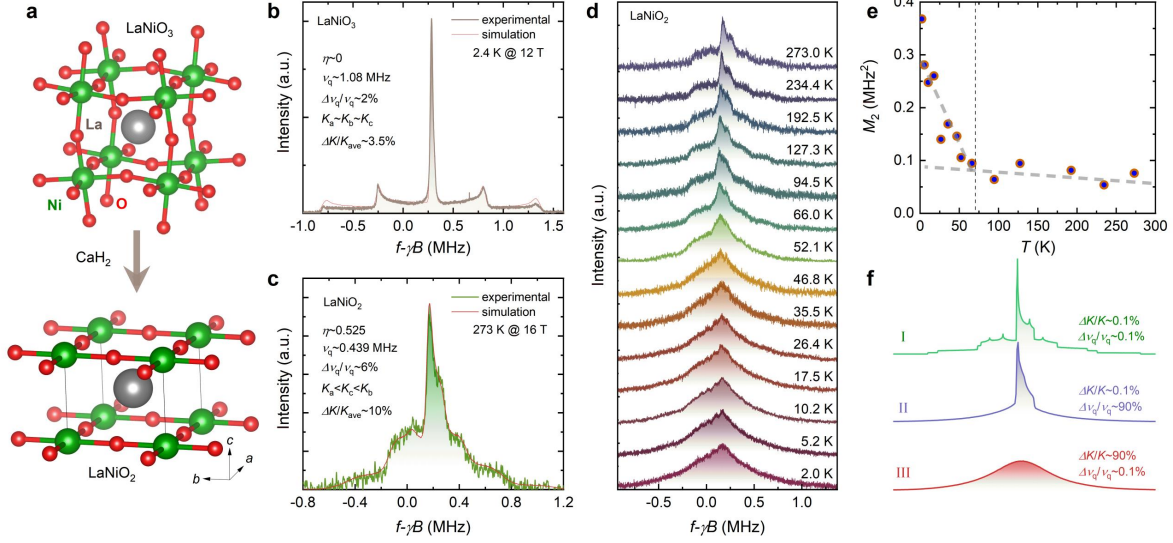


FIG. 1. **Crystal structure and temperature-dependent ^{17}O NMR spectra in LaNiO_2 .**

(a) Sketch of the structural change from LaNiO_3 to LaNiO_2 by topotactic reduction with metal hydride CaH_2 . (b-c) NMR spectra of LaNiO_3 and LaNiO_2 . The solid red curve represents the simulation result. The asymmetry factor $\eta = \left| \frac{V_{cc} - V_{aa}}{V_{bb}} \right|$ characterizes the asymmetry of the electric field gradient, where $V_{\alpha\alpha} = \frac{\partial^2 V}{\partial \alpha^2}$ ($\alpha = a, b$, and c) represents the second derivative of the electric potential at the ^{17}O nuclei along the three crystallographic directions. K_a , K_b and K_c describe the Knight shifts along the three crystallographic directions (for details, see Sec. S3 in the Supplemental Information). (d) ^{17}O full spectra of LaNiO_2 at temperatures from 2.0 K to 273.0 K at a fixed field of $B \sim 16$ T. (e) Temperature-dependent second central moment of the ^{17}O spectra of LaNiO_2 . (f) Simulation of the broadening effect in ^{17}O spectra.

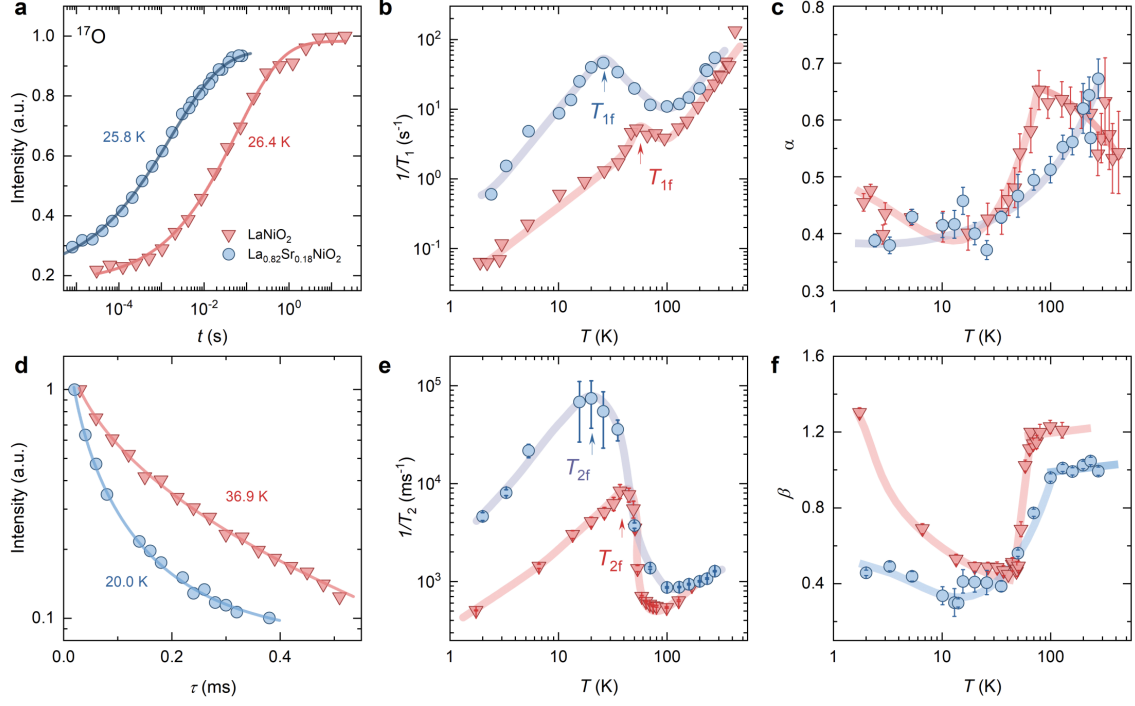


FIG. 2. **NMR relaxation evidence for glassy spin dynamics in LaNiO_2 and $\text{La}_{0.82}\text{Sr}_{0.18}\text{NiO}_2$.** (a) Time dependence of ^{17}O nuclear magnetization $M(t) = M_z(t)/M_z(\infty)$ after a comb of $\pi/2$ saturation pulses in LaNiO_2 and $\text{La}_{0.82}\text{Sr}_{0.18}\text{NiO}_2$. By fitting the relaxation curves via the stretched exponential form $M(t) = M_0 + M_1 \left(0.028e^{-\left(\frac{t}{T_1}\right)^\alpha} + 0.178e^{-\left(\frac{6t}{T_1}\right)^\alpha} + 0.794e^{-\left(\frac{15t}{T_1}\right)^\alpha} \right)$, we extracted both the spin-lattice relaxation time T_1 and the stretching exponent α . (b) The temperature-dependent spin-lattice relaxation rate $1/T_1$ for ^{17}O in LaNiO_2 and $\text{La}_{0.82}\text{Sr}_{0.18}\text{NiO}_2$ (c) The temperature-dependent stretching factor α in LaNiO_2 and $\text{La}_{0.82}\text{Sr}_{0.18}\text{NiO}_2$. (d) The spin-echo decay curves of ^{17}O in LaNiO_2 and $\text{La}_{0.82}\text{Sr}_{0.18}\text{NiO}_2$. (e) The temperature-dependent spin-spin relaxation rate $1/T_2$ for ^{17}O in LaNiO_2 and $\text{La}_{0.82}\text{Sr}_{0.18}\text{NiO}_2$. (f) The temperature-dependent factor β in LaNiO_2 and $\text{La}_{0.82}\text{Sr}_{0.18}\text{NiO}_2$

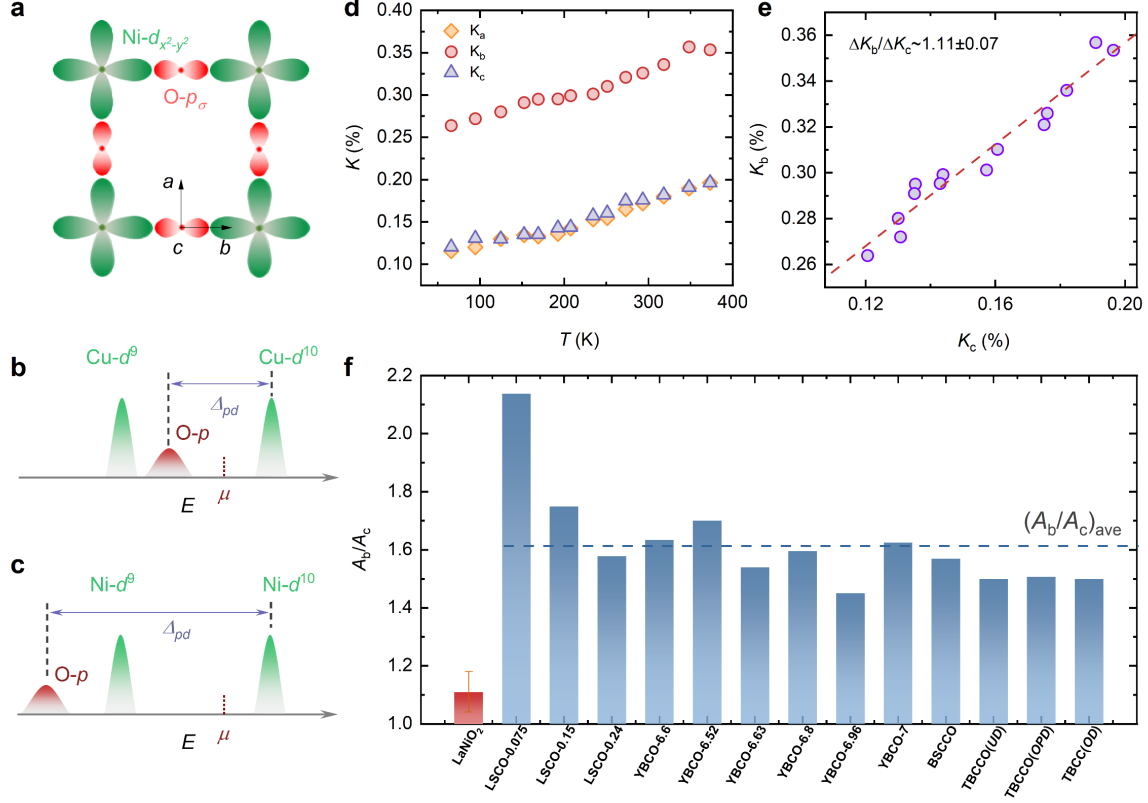


FIG. 3. Knight shift analysis of superexchange interactions. (a) Sketch of Ni- d orbitals and O- p orbitals in NiO_2 plane. (b)-(c) Schematic of the Zaanen-Sawatzky-Allen electronic structure comparison between the infinite-layer nickelates and cuprates, showing the O- p , Ni- d and Cu- d states. This illustrates the increase in nickelate charge-transfer energy Δ_{pd} relative to the Coulomb repulsion U . (d) Temperature-dependent Knight shift ^{17}K along a , b and c directions. (e) $^{17}K_b$ versus $^{17}K_c$, which are extracted from the data in panel (d). The dashed line is a linear fit whose slope is 1.11 ± 0.07 . (f) Ratios of hyperfine coupling constants along b and c directions for LaNiO_2 in this work, as well as for a variety of cuprates based on literature data [76–82]. The blue dashed line shows the mean value of the A_b/A_c for cuprates.

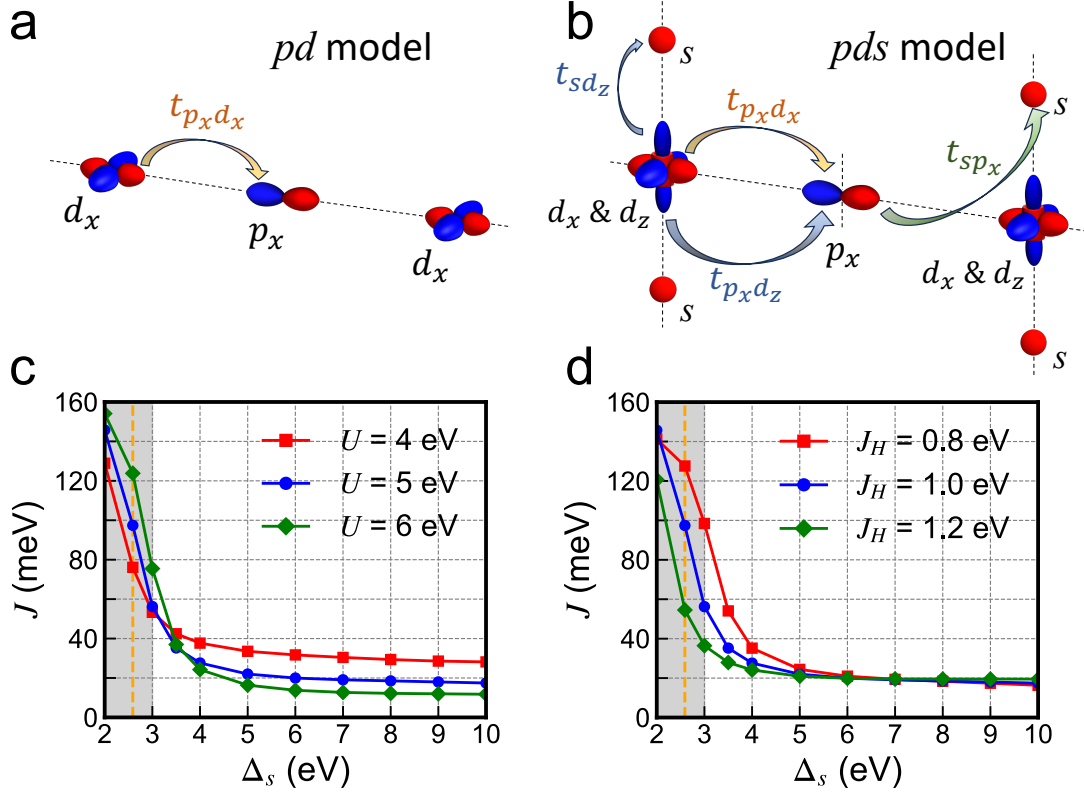


FIG. 4. **Modeling the superexchange in LaNiO_2 .** (a) The *pd* model, consisting of two $d_{x^2-y^2}$ orbitals and a central p_x orbital, capturing the conventional superexchange pathway via the *pd* σ -bond. (b) The extended *pds* model, comprising two correlated Ni sites. Each site hosts a Ni- $d_{x^2-y^2}$ and a Ni- $d_{3z^2-r^2}$ orbital, and is flanked by two interstitial s orbitals. A single O- p_x orbital is located between the two Ni sites. In both (a) and (b), d_x and d_z denote the Ni- $d_{x^2-y^2}$ and Ni- $d_{3z^2-r^2}$ orbitals, respectively. All symmetry-allowed nearest-neighbor hoppings $t_{\alpha\beta}$ between orbitals α and β are explicitly shown. (c) Superexchange coupling J as a function of the interstitial orbital energy Δ_s , calculated for several values of the Hubbard interaction U , with Hund's coupling fixed at $J_H = 0.2U$. (d) Superexchange J as a function of Δ_s , calculated for varying J_H values at fixed $U = 5$ eV.

-
- [1] D. Li, K. Lee, B. Y. Wang, M. Osada, S. Crossley, H. R. Lee, Y. Cui, Y. Hikita, and H. Y. Hwang, Superconductivity in an infinite-layer nickelate, *Nature* **572**, 624 (2019).
 - [2] M. Osada, B. Y. Wang, B. H. Goodge, S. P. Harvey, K. Lee, D. Li, L. F. Kourkoutis, and H. Y. Hwang, Nickelate superconductivity without rare-earth magnetism:(La,Sr)NiO₂, *Advanced Materials* **33**, 2104083 (2021).
 - [3] S. Zeng, C. Li, L. E. Chow, Y. Cao, Z. Zhang, C. S. Tang, X. Yin, Z. S. Lim, J. Hu, P. Yang, *et al.*, Superconductivity in infinite-layer nickelate La_{1-x}Ca_xNiO₂ thin films, *Science advances* **8**, eabl9927 (2022).
 - [4] M. Osada, B. Y. Wang, B. H. Goodge, K. Lee, H. Yoon, K. Sakuma, D. Li, M. Miura, L. F. Kourkoutis, and H. Y. Hwang, A superconducting praseodymium nickelate with infinite layer structure, *Nano letters* **20**, 5735 (2020).
 - [5] M. Jiang, M. Berciu, and G. A. Sawatzky, Critical Nature of the Ni Spin State in Doped NdNiO₂, *Phys. Rev. Lett.* **124**, 207004 (2020).
 - [6] D. Zhao, Y. B. Zhou, Y. Fu, L. Wang, X. F. Zhou, H. Cheng, J. Li, D. W. Song, S. J. Li, B. L. Kang, L. X. Zheng, L. P. Nie, Z. M. Wu, M. Shan, F. H. Yu, J. J. Ying, S. M. Wang, J. W. Mei, T. Wu, and X. H. Chen, Intrinsic Spin Susceptibility and Pseudogaplike Behavior in Infinite-Layer LaNiO₂, *Phys. Rev. Lett.* **126**, 197001 (2021).
 - [7] Y. Fu, L. Wang, H. Cheng, S. Pei, X. Zhou, J. Chen, S. Wang, R. Zhao, W. Jiang, C. Liu, *et al.*, Core-level x-ray photoemission and Raman spectroscopy studies on electronic structures in Mott-Hubbard type nickelate oxide NdNiO₂, *arXiv:1911.03177* (2019).
 - [8] R. A. Ortiz, P. Puphal, M. Klett, F. Hotz, R. K. Kremer, H. Trepka, M. Hemmida, H.-A. K. von Nidda, M. Isobe, R. Khasanov, *et al.*, Magnetic correlations in infinite-layer nickelates: An experimental and theoretical multimethod study, *Physical Review Research* **4**, 023093 (2022).
 - [9] J. Fowlie, M. Hadjimichael, M. M. Martins, D. Li, M. Osada, B. Y. Wang, K. Lee, Y. Lee, Z. Salman, T. Prokscha, *et al.*, Intrinsic magnetism in superconducting infinite-layer nickelates, *Nature Physics* **18**, 1043 (2022).
 - [10] H. Lin, D. J. Gawryluk, Y. M. Klein, S. Huangfu, E. Pomjakushina, F. von Rohr, and A. Schilling, Universal spin-glass behaviour in bulk LaNiO₂, PrNiO₂ and NdNiO₂, *New Journal of Physics* **24**, 013022 (2022).

- [11] H. Lu, M. Rossi, A. Nag, M. Osada, D. F. Li, K. Lee, B. Y. Wang, M. Garcia-Fernandez, S. Agrestini, Z. X. Shen, E. M. Been, B. Moritz, T. P. Devereaux, J. Zaanen, H. Y. Hwang, K.-J. Zhou, and W. S. Lee, Magnetic excitations in infinite-layer nickelates, *Science* **373**, 213 (2021).
- [12] G. Krieger, L. Martinelli, S. Zeng, L. E. Chow, K. Kummer, R. Arpaia, M. Moretti Sala, N. B. Brookes, A. Ariando, N. Viart, M. Salluzzo, G. Ghiringhelli, and D. Preziosi, Charge and Spin Order Dichotomy in Driven by the Capping Layer, *Phys. Rev. Lett.* **129**, 027002 (2022).
- [13] Q. Gao, S. Fan, Q. Wang, J. Li, X. Ren, I. Bialo, A. Drewanowski, P. Rothenbühler, J. Choi, R. Sutarto, *et al.*, Magnetic excitations in strained infinite-layer nickelate PrNiO_2 films, *Nat. Commun.* **15**, 5576 (2024).
- [14] S. Fan, H. LaBollita, Q. Gao, N. Khan, Y. Gu, T. Kim, J. Li, V. Bhartiya, Y. Li, W. Sun, J. Yang, S. Yan, A. Barbour, X. Zhou, A. Cano, F. Bernardini, Y. Nie, Z. Zhu, V. Bisogni, C. Mazzoli, A. S. Botana, and J. Pelliciari, Capping Effects on Spin and Charge Excitations in Parent and Superconducting $\text{Nd}_{1-x}\text{Sr}_x\text{NiO}_2$, *Phys. Rev. Lett.* **133**, 206501 (2024).
- [15] S. Hayashida, V. Sundaramurthy, P. Puphal, M. Garcia-Fernandez, K.-J. Zhou, B. Fenk, M. Isobe, M. Minola, Y.-M. Wu, Y. E. Suyolcu, P. A. van Aken, B. Keimer, and M. Hepting, Investigation of spin excitations and charge order in bulk crystals of the infinite-layer nickelate LaNiO_2 , *Phys. Rev. B* **109**, 235106 (2024).
- [16] M.-H. Julien, F. Borsa, P. Carretta, M. Horvatić, C. Berthier, and C. T. Lin, Charge segregation, cluster spin glass, and superconductivity in $\text{La}_{1.94}\text{Sr}_{0.06}\text{CuO}_4$, *Phys. Rev. Lett.* **83**, 604 (1999).
- [17] M.-H. Julien, A. Campana, A. Rigamonti, P. Carretta, F. Borsa, P. Kuhns, A. P. Reyes, W. G. Moulton, M. Horvatić, C. Berthier, A. Vietkin, and A. Revcolevschi, Glassy spin freezing and NMR wipeout effect in the high- T_c superconductor $\text{La}_{1.90}\text{Sr}_{0.10}\text{CuO}_4$: Critical discussion of the role of stripes, *Phys. Rev. B* **63**, 144508 (2001).
- [18] T. Wu, H. Mayaffre, S. Krämer, M. Horvatić, C. Berthier, C. T. Lin, D. Haug, T. Loew, V. Hinkov, B. Keimer, and M.-H. Julien, Magnetic-field-enhanced spin freezing on the verge of charge ordering in $\text{YBa}_2\text{Cu}_3\text{O}_{6.45}$, *Phys. Rev. B* **88**, 014511 (2013).
- [19] M. Frachet, I. Vinograd, R. Zhou, S. Benhabib, S. Wu, H. Mayaffre, S. Krämer, S. K. Ramakrishna, A. P. Reyes, J. Debray, *et al.*, Hidden magnetism at the pseudogap critical point of a cuprate superconductor, *Nat. Phys.* **16**, 1064 (2020).

- [20] S.-H. Baek, T. Loew, V. Hinkov, C. T. Lin, B. Keimer, B. Büchner, and H.-J. Grafe, Evidence of a critical hole concentration in underdoped $\text{YBa}_2\text{Cu}_3\text{O}_y$ single crystals revealed by ^{63}Cu NMR, *Phys. Rev. B* **86**, 220504 (2012).
- [21] N. J. Curro, P. C. Hammel, B. J. Suh, M. Hücker, B. Büchner, U. Ammerahl, and A. Revcolevschi, Inhomogeneous Low Frequency Spin Dynamics in $\text{La}_{1.65}\text{Eu}_{0.2}\text{Sr}_{0.15}\text{CuO}_4$, *Phys. Rev. Lett.* **85**, 642 (2000).
- [22] A. Arsenault, S. Takahashi, T. Imai, W. He, Y. Lee, and M. Fujita, ^{139}La NMR investigation of the charge and spin order in a $\text{La}_{1.885}\text{Sr}_{0.115}\text{CuO}_4$ single crystal, *Physical Review B* **97**, 064511 (2018).
- [23] B. J. Suh, P. C. Hammel, M. Hücker, B. Büchner, U. Ammerahl, and A. Revcolevschi, Spin dynamics in the low-temperature tetragonal phase of $\cong \frac{1}{8}$ doped single crystal $\text{La}_{1.67}\text{Eu}_{0.2}\text{Sr}_{0.13}\text{CuO}_4$, *Phys. Rev. B* **61**, R9265 (2000).
- [24] V. F. Mitrović, M.-H. Julien, C. de Vaulx, M. Horvatić, C. Berthier, T. Suzuki, and K. Yamada, Similar glassy features in the ^{139}La NMR response of pure and disordered $\text{La}_{1.88}\text{Sr}_{0.12}\text{CuO}_4$, *Phys. Rev. B* **78**, 014504 (2008).
- [25] G. B. Teitel'baum, I. M. Abu-Shiekh, O. Bakharev, H. B. Brom, and J. Zaanen, Spin dynamics and ordering of a cuprate stripe antiferromagnet, *Phys. Rev. B* **63**, 020507 (2000).
- [26] A. W. Hunt, P. M. Singer, A. F. Cederström, and T. Imai, Glassy slowing of stripe modulation in $(\text{La},\text{Eu},\text{Nd})_{2-x}(\text{Sr},\text{Ba})_x\text{CuO}_4$: A ^{63}Cu and ^{139}La NQR study down to 350 mK, *Phys. Rev. B* **64**, 134525 (2001).
- [27] S.-H. Baek, A. Erb, and B. Büchner, Low-energy spin dynamics and critical hole concentrations in $\text{La}_{2-x}\text{Sr}_x\text{CuO}_4$ ($0.07 \leq x \leq 0.2$) revealed by ^{139}La and ^{63}Cu nuclear magnetic resonance, *Phys. Rev. B* **96**, 094519 (2017).
- [28] S.-H. Baek, Y. Utz, M. Hücker, G. D. Gu, B. Büchner, and H.-J. Grafe, Magnetic field induced anisotropy of ^{139}La spin-lattice relaxation rates in stripe ordered $\text{La}_{1.875}\text{Ba}_{0.125}\text{CuO}_4$, *Phys. Rev. B* **92**, 155144 (2015).
- [29] J. H. Cho, F. Borsa, D. C. Johnston, and D. R. Torgeson, Spin dynamics in $\text{La}_{2-x}\text{Sr}_x\text{CuO}_4$ ($0.02 \leq x \leq 0.08$) from ^{139}La NQR relaxation: Fluctuations in a finite-length-scale system, *Phys. Rev. B* **46**, 3179 (1992).
- [30] M. H. Julien, P. Carretta, and F. Borsa, NQR study of spin-freezing in superconducting $\text{La}_{2-x}\text{Sr}_x\text{CuO}_4$: the example of $x = 0.06$, *Applied Magnetic Resonance* **19**, 287 (2000).

- [31] I. Vinograd, R. Zhou, H. Mayaffre, S. Krämer, S. K. Ramakrishna, A. P. Reyes, T. Kurosawa, N. Momono, M. Oda, S. Komiya, S. Ono, M. Horio, J. Chang, and M.-H. Julien, Competition between spin ordering and superconductivity near the pseudogap boundary in $\text{La}_{2-x}\text{Sr}_x\text{CuO}_4$: Insights from NMR, *Phys. Rev. B* **106**, 054522 (2022).
- [32] A. Missiaen, H. Mayaffre, S. Krämer, D. Zhao, Y. Zhou, T. Wu, X. Chen, S. Pyon, T. Takayama, H. Takagi, D. LeBoeuf, and M.-H. Julien, Spin-Stripe Order Tied to the Pseudogap Phase in $\text{La}_{1.8-x}\text{Eu}_{0.2}\text{Sr}_x\text{CuO}_4$, *Phys. Rev. X* **15**, 021010 (2025).
- [33] N. Bloembergen, E. M. Purcell, and R. V. Pound, Relaxation Effects in Nuclear Magnetic Resonance Absorption, *Phys. Rev.* **73**, 679 (1948).
- [34] P. Lepucki, R. Havemann, A. P. Dioguardi, F. Scaravaggi, A. U. B. Wolter, R. Kappenberger, S. Aswartham, S. Wurmehl, B. Büchner, and H.-J. Grafe, Mapping out the spin fluctuations in Co-doped LaFeAsO single crystals by NMR, *Phys. Rev. B* **103**, L180506 (2021).
- [35] R. J. Birgeneau, C. Stock, J. M. Tranquada, and K. Yamada, Magnetic neutron scattering in hole-doped cuprate superconductors, *J. Phys. Soc. Jpn.* **75**, 111003 (2006).
- [36] M. Le Tacon, G. Ghiringhelli, J. Chaloupka, M. M. Sala, V. Hinkov, M. Haverkort, M. Minola, M. Bakr, K. Zhou, S. Blanco-Canosa, *et al.*, Intense paramagnon excitations in a large family of high-temperature superconductors, *Nat. Phys.* **7**, 725 (2011).
- [37] M. Dean, G. Dellea, R. S. Springell, F. Yakhov-Harris, K. Kummer, N. Brookes, X. Liu, Y. Sun, J. Strle, T. Schmitt, *et al.*, Persistence of magnetic excitations in $\text{La}_{2-x}\text{Sr}_x\text{CuO}_4$ from the undoped insulator to the heavily overdoped non-superconducting metal, *Nat. Mater.* **12**, 1019 (2013).
- [38] M. Minola, G. Dellea, H. Gretarsson, Y. Y. Peng, Y. Lu, J. Porras, T. Loew, F. Yakhov, N. B. Brookes, Y. B. Huang, J. Pellicciari, T. Schmitt, G. Ghiringhelli, B. Keimer, L. Braicovich, and M. Le Tacon, Collective nature of spin excitations in superconducting cuprates probed by resonant inelastic x-ray scattering, *Phys. Rev. Lett.* **114**, 217003 (2015).
- [39] G.-M. Zhang, Y.-f. Yang, and F.-C. Zhang, Self-doped Mott insulator for parent compounds of nickelate superconductors, *Phys. Rev. B* **101**, 020501 (2020).
- [40] J. Zaanen and G. Sawatzky, The electronic structure and superexchange interactions in transition-metal compounds, *Can. J. Phys.* **65**, 1262 (1987).
- [41] A. Abragam and B. Bleaney, *Electron Paramagnetic Resonance of Transition Ions* (Oxford Univ. Press, 2013).

- [42] M. Takigawa, A. P. Reyes, P. C. Hammel, J. D. Thompson, R. H. Heffner, Z. Fisk, and K. C. Ott, Cu and O NMR studies of the magnetic properties of $\text{YBa}_2\text{Cu}_3\text{O}_{6.63}$ ($T_c=62$ K), *Phys. Rev. B* **43**, 247 (1991).
- [43] R. E. Walstedt, *The NMR Probe of High- T_c Materials* (Springer Berlin Heidelberg, 2008).
- [44] L. Wang, G. He, Z. Yang, M. Garcia-Fernandez, A. Nag, K. Zhou, M. Minola, M. L. Tacon, B. Keimer, Y. Peng, *et al.*, Paramagnons and high-temperature superconductivity in a model family of cuprates, *Nat. Commun.* **13**, 3163 (2022).
- [45] M. Le Tacon, M. Minola, D. C. Peets, M. Moretti Sala, S. Blanco-Canosa, V. Hinkov, R. Liang, D. A. Bonn, W. N. Hardy, C. T. Lin, T. Schmitt, L. Braicovich, G. Ghiringhelli, and B. Keimer, Dispersive spin excitations in highly overdoped cuprates revealed by resonant inelastic x-ray scattering, *Phys. Rev. B* **88**, 020501(R) (2013).
- [46] M. Hepting, D. Li, C. Jia, H. Lu, E. Paris, Y. Tseng, X. Feng, M. Osada, E. Been, Y. Hikita, *et al.*, Electronic structure of the parent compound of superconducting infinite-layer nickelates, *Nat. Mater.* **19**, 381 (2020).
- [47] Z. Liu, Z. Ren, W. Zhu, Z. Wang, and J. Yang, Electronic and magnetic structure of infinite-layer NdNiO_2 : trace of antiferromagnetic metal, *npj Quantum Materials* **5**, 31 (2020).
- [48] Y. Gu, S. Zhu, X. Wang, J. Hu, and H. Chen, A substantial hybridization between correlated Ni- d orbital and itinerant electrons in infinite-layer nickelates, *Communications Physics* **3**, 84 (2020).
- [49] H. Chen, Y.-f. Yang, G.-M. Zhang, and H. Liu, An electronic origin of charge order in infinite-layer nickelates, *Nat. Commun.* **14**, 5477 (2023).
- [50] T. Y. Xie, Z. Liu, C. Cao, Z. F. Wang, J. L. Yang, and W. Zhu, Microscopic theory of superconducting phase diagram in infinite-layer nickelates, *Phys. Rev. B* **106**, 035111 (2022).
- [51] X. Chen, J. Choi, Z. Jiang, J. Mei, K. Jiang, J. Li, S. Agrestini, M. Garcia-Fernandez, H. Sun, X. Huang, *et al.*, Electronic and magnetic excitations in $\text{La}_3\text{Ni}_2\text{O}_7$, *Nat. Commun.* **15**, 9597 (2024).
- [52] M. Jiang, M. Berciu, and G. A. Sawatzky, Stabilization of singlet hole-doped state in infinite-layer nickelate superconductors, *Phys. Rev. B* **106**, 115150 (2022).
- [53] J. Kanamori, Electron Correlation and Ferromagnetism of Transition Metals, *Progress of Theoretical Physics* **30**, 275 (1963).

- [54] F. Petocchi, V. Christiansson, F. Nilsson, F. Aryasetiawan, and P. Werner, Normal State of $\text{Nd}_{1-x}\text{Sr}_x\text{NiO}_2$ from Self-Consistent $GW + \text{EDMFT}$, *Phys. Rev. X* **10**, 041047 (2020).
- [55] P. A. Lee, N. Nagaosa, and X.-G. Wen, Doping a Mott insulator: Physics of high-temperature superconductivity, *Rev. Mod. Phys.* **78**, 17 (2006).
- [56] D. J. Scalapino, A common thread: The pairing interaction for unconventional superconductors, *Rev. Mod. Phys.* **84**, 1383 (2012).
- [57] Z. Wang, C. Zou, C. Lin, X. Luo, H. Yan, C. Yin, Y. Xu, X. Zhou, Y. Wang, and J. Zhu, Correlating the charge-transfer gap to the maximum transition temperature in $\text{Bi}_2\text{Sr}_2\text{Ca}_{n-1}\text{Cu}_n\text{O}_{2n+4+\delta}$, *Science* **381**, 227 (2023).
- [58] S. Chow, Z. Luo, and A. Ariando, Bulk superconductivity near 40 K in hole-doped SmNiO_2 at ambient pressure, *Nature* (2025).
- [59] F. Deganello, G. Marci, and G. Deganello, Citrate–nitrate auto-combustion synthesis of perovskite-type nanopowders: A systematic approach, *Journal of the European Ceramic Society* **29**, 439 (2009).
- [60] T. Takamatsu, M. Kato, T. Noji, and Y. Koike, Low-temperature synthesis of the infinite-layer compound LaNiO_2 by soft-chemical techniques, *Japanese Journal of Applied Physics* **49**, 093101 (2010).
- [61] P. Hohenberg and W. Kohn, Inhomogeneous electron gas, *Phys. Rev.* **136**, B864 (1964).
- [62] W. Kohn and L. J. Sham, Self-consistent equations including exchange and correlation effects, *Phys. Rev.* **140**, A1133 (1965).
- [63] G. Kresse and J. Furthmüller, Efficient iterative schemes for ab initio total-energy calculations using a plane-wave basis set, *Phys. Rev. B* **54**, 11169 (1996).
- [64] G. Kresse and D. Joubert, From ultrasoft pseudopotentials to the projector augmented-wave method, *Phys. Rev. B* **59**, 1758 (1999).
- [65] J. P. Perdew, K. Burke, and M. Ernzerhof, Generalized gradient approximation made simple, *Phys. Rev. Lett.* **77**, 3865 (1996).
- [66] N. Marzari, A. A. Mostofi, J. R. Yates, I. Souza, and D. Vanderbilt, Maximally localized wannier functions: Theory and applications, *Rev. Mod. Phys.* **84**, 1419 (2012).
- [67] A. A. Mostofi, J. R. Yates, Y.-S. Lee, I. Souza, D. Vanderbilt, and N. Marzari, wannier90: A tool for obtaining maximally-localised wannier functions, *Computer Physics Communications* **178**, 685 (2008).

- [68] A. Georges, G. Kotliar, W. Krauth, and M. J. Rozenberg, Dynamical mean-field theory of strongly correlated fermion systems and the limit of infinite dimensions, *Rev. Mod. Phys.* **68**, 13 (1996).
- [69] G. Kotliar, S. Y. Savrasov, K. Haule, V. S. Oudovenko, O. Parcollet, and C. A. Marianetti, Electronic structure calculations with dynamical mean-field theory, *Rev. Mod. Phys.* **78**, 865 (2006).
- [70] P. Werner, A. Comanac, L. de' Medici, M. Troyer, and A. J. Millis, Continuous-time solver for quantum impurity models, *Phys. Rev. Lett.* **97**, 076405 (2006).
- [71] E. Gull, A. J. Millis, A. I. Lichtenstein, A. N. Rubtsov, M. Troyer, and P. Werner, Continuous-time monte carlo methods for quantum impurity models, *Rev. Mod. Phys.* **83**, 349 (2011).
- [72] K. Haule, Quantum monte carlo impurity solver for cluster dynamical mean-field theory and electronic structure calculations with adjustable cluster base, *Phys. Rev. B* **75**, 155113 (2007).
- [73] P. Werner, E. Gull, and A. J. Millis, Metal-insulator phase diagram and orbital selectivity in three-orbital models with rotationally invariant hund coupling, *Phys. Rev. B* **79**, 115119 (2009).
- [74] M. T. Czyżyk and G. A. Sawatzky, Local-density functional and on-site correlations: The electronic structure of La_2CuO_4 and LaCuO_3 , *Phys. Rev. B* **49**, 14211 (1994).
- [75] H. T. Dang, J. Mravlje, A. Georges, and A. J. Millis, Electronic correlations, magnetism, and hund's rule coupling in the ruthenium perovskites SrRuO_3 and CaRuO_3 , *Phys. Rev. B* **91**, 195149 (2015).
- [76] M. Takigawa, P. C. Hammel, R. H. Heffner, Z. Fisk, K. C. Ott, and J. D. Thompson, ^{17}O NMR study of local spin susceptibility in aligned $\text{YBa}_2\text{Cu}_3\text{O}_7$ powder, *Phys. Rev. Lett.* **63**, 1865 (1989).
- [77] G.-Q. Zheng, T. Kuse, Y. Kitaoka, K. Ishida, S. Ohsugi, K. Asayama, and Y. Yamada, ^{17}O NMR study of $\text{La}_{2-x}\text{Sr}_x\text{CuO}_4$ in the lightly-and heavily-doped regions, *Physica C: Superconductivity* **208**, 339 (1993).
- [78] Y. Yoshinari, H. Yasuoka, Y. Ueda, K.-i. Koga, and K. Kosuge, NMR Studies of ^{17}O in the Normal State of $\text{YBa}_2\text{Cu}_3\text{O}_{6+x}$, *J. Phys. Soc. Jpn.* **59**, 3698 (1990).
- [79] M. Horvatić, C. Berthier, Y. Berthier, P. Ségransan, P. Butaud, W. G. Clark, J. A. Gillet, and J. Y. Henry, Nuclear-spin-lattice relaxation rate of planar oxygen in $\text{YBa}_2\text{Cu}_3\text{O}_{6.52}$ and $\text{YBa}_{1.92}\text{Sr}_{0.08}\text{Cu}_3\text{O}_7$ single crystals, *Phys. Rev. B* **48**, 13848 (1993).

- [80] J. A. Martindale, P. C. Hammel, W. L. Hults, and J. L. Smith, Temperature dependence of the anisotropy of the planar oxygen nuclear spin-lattice relaxation rate in $\text{YBa}_2\text{Cu}_3\text{O}_y$, *Phys. Rev. B* **57**, 11769 (1998).
- [81] J. Crocker, A. P. Dioguardi, N. apRoberts Warren, A. C. Shockley, H.-J. Grafe, Z. Xu, J. Wen, G. Gu, and N. J. Curro, NMR studies of pseudogap and electronic inhomogeneity in $\text{Bi}_2\text{Sr}_2\text{CaCu}_2\text{O}_{8+\delta}$, *Phys. Rev. B* **84**, 224502 (2011).
- [82] A. Gerashenko, Y. Piskunov, K. Mikhalev, A. Ananyev, K. Okulova, S. Verkhovskii, A. Yakubovskii, L. Shustov, and A. Trokiner, The ^{63}Cu and ^{17}O NMR studies of spin susceptibility in differently doped $\text{Tl}_2\text{Ba}_2\text{CaCu}_2\text{O}_{8-\delta}$ compounds, *Physica C: Superconductivity* **328**, 163 (1999).